Singular forces and pointlike colloids in lattice Boltzmann hydrodynamics

R. W. Nash,[1] R. Adhikari,[2,1] and M. E. Cates[1]
[1]*SUPA, School of Physics, The University of Edinburgh, JCMB King's Buildings, Edinburgh EH9 3JZ, United Kingdom*
[2]*The Institute of Mathematical Sciences, CIT Campus, Tharamani, Chennai 600113, India*
(Received 9 July 2007; revised manuscript received 19 October 2007; published 27 February 2008)

We present an accurate method to include arbitrary singular distributions of forces in the lattice Boltzmann formulation of hydrodynamics. We validate our method with several examples involving Stokeslet, stresslet, and rotlet singularities, finding excellent agreement with analytical results. A minimal model for sedimenting particles is presented using the method. In the dilute limit, this model has accuracy comparable to, but computational efficiency much greater than, algorithms that explicitly resolve the size of the particles.

DOI: 10.1103/PhysRevE.77.026709 PACS number(s): 47.11.−j, 47.15.G−, 82.70.Dd

I. INTRODUCTION

The numerical integration of the discrete-velocity Boltzmann equation provides an efficient method for the solution of isothermal, incompressible fluid flows in complex geometries [1]. The finite-difference equation generated by the integration scheme is referred to as the lattice Boltzmann equation (LBE). The method can be extended to study multiphase [2,3] and multicomponent [4] flows, the hydrodynamics of polymers [5] and suspensions [6,7], and flows under gravity [8]. In these extensions of the LBE, the resulting momentum balance equations contain additional terms beyond the usual pressure and viscous forces. These represent forces acting on the fluid, either from external sources like gravity, or internal sources like the gas-liquid interface in a two-phase fluid.

The LBE, derived as it is from the Boltzmann equation for a dilute gas, can only faithfully represent the hydrodynamics of a fluid with an ideal-gas equation of state and a Newtonian constitutive equation [9]. One way around this restrictive situation is to use the forced Boltzmann equation to represent the additional forces that appear in the extensions described above [1]. So far, this idea has been used mainly to model the effects of gravity [8] and gas-liquid interfacial forces in nonideal gases [3]. These correspond to two special types of force distribution: in the case of gravity, the force is spatially and temporally constant, while in the case of the gas-liquid interface, the force varies both in space and time, but is evaluated only on the nodes of the computational grid. The forces in either case are *smooth* functions of position.

However, many models of boundaries immersed in fluids require *singular* distributions of forces. Such a description follows, for example, when a gas-liquid interface is described as a two-dimensional manifold of zero thickness instead of a three-dimensional volume of space where the density changes rapidly. In a similar mathematical idealization, a polymer in a fluid may be represented as a one-dimensional curve with a singular distribution of forces [10]. In yet another example, at distances large compared to its radius, a sedimenting colloid can be well approximated as a singular point force [11]. Clearly, the range of applications of lattice Boltzmann hydrodynamics can be greatly expanded if singular force densities, not necessarily located at grid points, can be incorporated into the method.

In this paper we address the inclusion of singular force densities. To do this, we first present a derivation of various results (largely available elsewhere) on how to incorporate forcing distributions that are smooth on the lattice scale. We then marry these to an established procedure for representing singular distributions, such as the δ function, on the lattice. Unless the singularity coincides with a lattice site, any interpolation of a singular distribution onto the lattice of course implies some smoothing. Importantly, however, there is a numerically optimal way to do this, which we adopt. The result is a systematic procedure for representating general force densities, having smooth and/or singular components, within the lattice Boltzmann formulation of hydrodynamics.

Since the LBE works with molecular velocity distribution functions at a mesoscopic scale, it is important to recognize what our singular force densities physically describe. They do not describe forces applied to a single fluid molecule, but instead represent forces localized within a region large compared to the molecular scale, but too small for the lattice to resolve. This representation is particularly useful for dilute colloids: these are pointlike on the scale of their separation, but if each such colloid is fully resolved (occupying several lattice cells) this separation becomes large on the lattice scale, so that the number of particles that can be simulated in practice is quite limited. Shrinking the colloids to a sublattice scale, and interpolating the resulting point forces optimally, allows a far higher number of colloids to be simulated because the mean spacing between particles can be of the order of one lattice site even for volume fractions of 1% or less. Such dilute colloids, when undergoing sedimentation, show many interesting features that apparently involve structuring of the system on scales much larger than the interparticle spacing [12]. As shown by the benchmark tests described below, our method promises accurate and efficient simulation on such scales, which may in future assist exploration of such physics.

In the following section we first discuss the discrete representation of the forcing term in the Boltzmann equation and derive a second-order accurate integration scheme for the discrete velocity forced Boltzmann equation using the method of characteristics. In Sec. III we introduce a general distribution of singular forces and using a suitable regularization of the δ function obtain a smooth but sharply peaked distribution of forces. The method is exemplified in Sec. III for three common singular force distributions (a Stokeslet, a

stresslet, and a rotlet) and validated for the Stokeslet case by comparison with a fully resolved numerical simulation. Finally, we show how our method can be adapted to provide a simplified description of a dilute suspension of sedimenting colloids. We end with a summary of our method and discuss potential applications.

II. MULTIPLE-RELAXATION-TIME FORCED LATTICE BOLTZMANN EQUATION

The LBE may be derived from the Boltzmann equation by a two-step procedure. First, a discrete-velocity Boltzmann equation (DVBE) is obtained by retaining a finite number of terms in the Hermite expansion of the Boltzmann equation and evaluating the integrals corresponding to the conserved moments using a Gauss quadrature [13–15]; see also [16,17]. The discrete velocities $\{\mathbf{c}_i\}$ are the nodes of the Gauss-Hermite quadrature. This is followed by a discretization in space and time to provide a numerical integration scheme, which is commonly called the LBE [18].

Usually a first-order explicit Euler scheme is used to integrate the DVBE, which surprisingly enough, gives second-order accurate results [18,19]. This is so because the discretization error has the same structure as the viscous term in the Navier-Stokes equation, whereby it can be absorbed by a simple redefinition of the viscosity to give second-order accuracy. The same Euler scheme for the forced Boltzmann equation gives a discretization error term which can be absorbed only by redefining physical quantities like the momentum and stress [20]. Below, we provide a straightforward explanation of these redefinitions and show how they are related to the discretization error induced by the integration scheme.

We begin with the discrete velocity Boltzmann equation including an external acceleration field $\mathbf{F}(\mathbf{x},t)$

$$\partial_t f_i + \mathbf{c}_i \cdot \boldsymbol{\nabla} f_i + [\mathbf{F} \cdot \boldsymbol{\nabla}_{\mathbf{c}} f]_i = -\mathcal{L}_{ij}(f_j - f_j^0), \tag{1}$$

where $f_i(\mathbf{x},t)$ is the one-particle distribution function in phase space of coordinates $\mathbf{x}$ and velocities $\mathbf{c}_i$, $\mathcal{L}_{ij}$ is the collision matrix linearized about the local equilibrium f_i^0, and the repeated index j is summed over. Mass and momentum conservation require the collision term to satisfy

$$\sum_{i=0}^{n} \mathcal{L}_{ij}(f_j - f_j^0) = 0, \quad \sum_{i=0}^{n} \mathcal{L}_{ij}(f_j - f_j^0)\mathbf{c}_i = \mathbf{0}, \tag{2}$$

while isotropy requires that the $\mathcal{L}_{ij}$ depend only on the angles between $\mathbf{c}_i$ and $\mathbf{c}_j$ [1]. Equation (1) is most easily derived by expanding the distribution functions in terms of tensor Hermite polynomials, truncating the expansion at a certain order, and evaluating the expansion coefficients using a Gaussian quadrature [21]. In d dimensions, the quadrature is defined by the n discrete velocities $\mathbf{c}_i$ and a set of weights w_i giving rise to a *DdQn* discrete Boltzmann equation [22]. Retaining terms up to second order in the Hermite expansion is sufficient for isothermal fluid flow problems. The equilibrium distribution functions to second order in the Hermite expansions are

$$f_i^0(\rho,\mathbf{v}) = w_i\left(\rho + \frac{\rho\mathbf{v}\cdot\mathbf{c}_i}{c_s^2} + \frac{\rho\mathbf{v}\mathbf{v}:\mathbf{Q}_i}{2c_s^4}\right), \tag{3}$$

where the tensor $Q_{i\alpha\beta} \equiv c_{i\alpha}c_{i\beta} - c_s^2\delta_{\alpha\beta}$ (where Greek indices denote Cartesian directions) and c_s is the speed of sound. The mass density ρ and the momentum density $\rho\mathbf{v}$ are moments of the distribution function:

$$\rho = \sum_{i=0}^{n} f_i, \quad \rho\mathbf{v} = \sum_{i=0}^{n} f_i\mathbf{c}_i. \tag{4}$$

To the same order, the discrete representation of the forcing term is given by [23]

$$[\mathbf{F}\cdot\boldsymbol{\nabla}_{\mathbf{c}} f]_i = -\rho w_i\left(\frac{\mathbf{F}\cdot\mathbf{c}_i}{c_s^2} + \frac{(\mathbf{v}\mathbf{F}+\mathbf{F}\mathbf{v}):\mathbf{Q}_i}{2c_s^4}\right) \equiv -\Phi_i(\mathbf{x},t). \tag{5}$$

This differs from the expression assumed in [24] [their Eq. (6)], which is not consistently second order in the Hermite expansion. Finally, the deviatoric momentum flux tensor

$$S_{\alpha\beta} = \Pi_{\alpha\beta} - \rho c_s^2\delta_{\alpha\beta} = \sum_{i=0}^{n} f_i Q_{i\alpha\beta} \tag{6}$$

is the second moment of the distribution function. In isothermal models, the higher moments represent nonconserved kinetic degrees of freedom, commonly known as ghost modes. In the hydrodynamic limit, Eq. (1) gives rise to Navier-Stokes behavior, described by

$$\rho(\partial_t\mathbf{v} + \mathbf{v}\cdot\boldsymbol{\nabla}\mathbf{v}) = -\boldsymbol{\nabla}p + \eta\nabla^2\mathbf{v} + \zeta\,\boldsymbol{\nabla}(\boldsymbol{\nabla}\cdot\mathbf{v}) + \mathbf{F}, \tag{7}$$

where the pressure obeys $p=\rho c_s^2$, and the shear viscosity η and the bulk viscosity ζ are related to the eigenvalues of $\mathcal{L}_{ij}$. In practice, the algorithm is normally used in a parameter regime where the fluid is nearly incompressible ($\nabla\cdot\mathbf{v}\simeq 0$).

To begin our derivation of the numerical scheme we rearrange Eq. (1) to obtain

$$\partial_t f_i + \mathbf{c}_i\cdot\boldsymbol{\nabla} f_i = R_i(\mathbf{x},t), \tag{8}$$

where $R_i(\mathbf{x},t) = -\mathcal{L}_{ij}[f_j(\mathbf{x},t) - f_j^0(\mathbf{x},t)] + \Phi_i(\mathbf{x},t)$ represents the effects of both collisions and forcing. Equation (8) represents a set of first-order hyperbolic equations and can be integrated using the method of characteristics [25]. Integrating over a time interval Δt we have

$$f_i(\mathbf{x}+\mathbf{c}_i\Delta t, t+\Delta t) - f_i(\mathbf{x},t) = \int_0^{\Delta t} ds\, R_i(\mathbf{x}+\mathbf{c}_i s, t+s). \tag{9}$$

The integral above may be approximated to second-order accuracy using the trapezium rule and the resulting terms transposed to give a set of implicit equations for the f_i:

$$f_i(\mathbf{x}+\mathbf{c}_i\Delta t, t+\Delta t) - \frac{\Delta t}{2}R_i(\mathbf{x}+\mathbf{c}_i\Delta t, t+\Delta t)$$

$$= f_i(\mathbf{x},t) - \frac{\Delta t}{2}R_i(\mathbf{x},t) + \Delta t R_i(\mathbf{x},t). \tag{10}$$

The structure of the above set of equations suggests the in-

troduction of a new set of *auxiliary* distribution functions [3,26]

$$\bar{f}_i(\mathbf{x},t) = f_i(\mathbf{x},t) - \frac{\Delta t}{2} R_i(\mathbf{x},t), \tag{11}$$

in terms of which the previous set of equations are explicit,

$$\bar{f}_i(\mathbf{x}+\mathbf{c}_i\Delta t, t+\Delta t) = \bar{f}_i(\mathbf{x},t) + R_i(\mathbf{x},t)\Delta t. \tag{12}$$

This shows that the LBE evolution can be thought of as two separate processes: the first is a relaxational step in which the distributions $\bar{f}_i$ are relaxed to their "postcollisional" values $\bar{f}_i(\mathbf{x},t^*)$,

$$\bar{f}_i(\mathbf{x},t^*) = \bar{f}_i(\mathbf{x},t) + R_i(\mathbf{x},t)\Delta t, \tag{13}$$

followed by a propagation step in which the postcollisional distributions are propagated along a Lagrangian trajectory without further change,

$$\bar{f}_i(\mathbf{x}+\mathbf{c}_i\Delta t, t+\Delta t) = \bar{f}_i(\mathbf{x},t^*). \tag{14}$$

Thus the computational part of the method is most naturally framed in terms of the auxiliary distributions $\bar{f}_i$ and not the physical distribution functions f_i themselves. To obtain the postcollisional $\bar{f}_i$ without having to refer to the f_i, the latter must be eliminated from Eq. (12). Inverting the equations defining the $\bar{f}_i$ in Eq. (11), we obtain

$$R_i = \left(\mathbb{1} + \frac{\Delta t}{2}\mathcal{L}\right)^{-1}_{ij} [-\mathcal{L}_{jk}(\bar{f}_k - f_k^0) + \Phi_j(\mathbf{x},t)]. \tag{15}$$

Combining this with Eq. (12) we obtain a numerical scheme for the forced discrete Boltzmann equation with a general collision operator in terms of the $\bar{f}_i$:

$$\bar{f}_i(\mathbf{x}+\mathbf{c}_i\Delta t, t+\Delta t) = \bar{f}_i(\mathbf{x},t) + \left(\mathbb{1} + \frac{\Delta t}{2}\mathcal{L}\right)^{-1}_{ij} \times [-\mathcal{L}_{jk}(\bar{f}_k - f_k^0) + \Phi_j(\mathbf{x},t)]. \tag{16}$$

For a single-relaxation-time collision operator, where $\mathcal{L}_{ij} = \delta_{ij}/\tau$, this takes on a particularly simple form,

$$\bar{f}_i(\mathbf{x}+\mathbf{c}_i\Delta t, t+\Delta t) = \bar{f}_i(\mathbf{x},t) + \frac{\Delta t}{\tau + \Delta t/2}[-(\bar{f}_i - f_i^0) + \tau\Phi_i(\mathbf{x},t)], \tag{17}$$

a result obtained previously by a multiscale expansion of the LBE dynamics [27]. For a nondiagonal collision operator, the collision term is best evaluated in the moment basis. For example, using a collision operator in which the ghost modes are projected out and the stress modes relax at a rate τ^{-1}, the postcollisional $\bar{f}_i$ [i.e., the right-hand side of Eq. (16)] is given by

$$\bar{f}_i(\mathbf{x},t^*) = w_i\left(\rho + \frac{A_\alpha c_{i\alpha}}{c_s^2} + \frac{B_{\alpha\beta}Q_{i\alpha\beta}}{2c_s^4}\right), \tag{18}$$

where A_α, the momentum component of the postcollisional auxiliary distributions, is

$$A_\alpha = \sum_{i=0}^{n} \bar{f}_i c_{i\alpha} + \rho F_\alpha \Delta t, \tag{19}$$

and $B_{\alpha\beta}$, the stress component, is

$$B_{\alpha\beta} = \sum_{i=0}^{n} \bar{f}_i Q_{i\alpha\beta} + \frac{\Delta t}{\tau + \Delta t/2}\left(\sum_{i=0}^{n} \bar{f}_i Q_{i\alpha\beta} - \rho v_\alpha v_\beta + \tau(v_\alpha F_\beta + F_\alpha v_\beta)\right). \tag{20}$$

The hydrodynamic variables are moments of the physical distribution f_i, but can easily be obtained from the auxiliary distributions $\bar{f}_i$ used in the computation, using the transformation rule Eq. (11), the definitions of the macroscopic variables, Eq. (4), and the constraints of mass and momentum conservation, Eq. (2). We obtain

$$\rho = \sum_{i=0}^{n} \bar{f}_i, \tag{21a}$$

$$\rho v_\alpha = \sum_{i=0}^{n} \bar{f}_i c_{i\alpha} + \rho F_\alpha \frac{\Delta t}{2}, \tag{21b}$$

$$S_{\alpha\beta} = \sum_{i=0}^{n} \bar{f}_i Q_{i\alpha\beta} + \frac{\Delta t/2}{\tau + \Delta t/2}\left(\sum_{i=0}^{n} \bar{f}_i Q_{i\alpha\beta} - \rho v_\alpha v_\beta + \tau(v_\alpha F_\beta + F_\alpha v_\beta)\right). \tag{21c}$$

The equilibria can be reconstructed from ρ and $\rho\mathbf{v}$. What appear in the literature as redefinitions of momentum and stresses are shown in the above analysis to be discretization errors which vanish as $\Delta t \to 0$. This completes the description of the method for the numerical solution of the forced LBE. Verberg and Ladd have derived results equivalent to those above using a multiple scale analysis of the discrete LBE dynamics [20], but it is not clear to us whether their analysis admits singular force densities. However, the above derivation shows that these equations are a reliable starting point, independent of Verberg and Ladd's analysis.

The LBE can be extended to situations where the fluctuations in the fluid density and momentum are important [6]. A consistent discrete kinetic theory of fluctuations was presented in [28], which improves on an earlier algorithm due to Ladd [6], and produces thermodynamically accurate variances of the local mass and momentum densities. We return to the issue of noise below, when we address the representation of Brownian colloids as point particles (Sec. IV).

III. SINGULAR FORCE DENSITIES

In a wide variety of situations, as mentioned in the Introduction, force densities may need to be defined off lattice, and may in addition be singular. Mathematically, such a force density may be written as

$$\mathbf{F}(\mathbf{r}) = \int \mathbf{f}(\mathbf{R})\delta(\mathbf{r}-\mathbf{R})d\lambda, \tag{22}$$

where the force is localized to some manifold described parametrically as $\mathbf{r}=\mathbf{R}(\lambda)$, and $d\lambda$ is the measure on the manifold. Any numerical method that attempts to deal with such force distributions must be reconciled with the singular nature of the force and, for grid-based numerical methods, the fact that the position of the manifold need not coincide with the nodes of the grid. In a well-established numerical method [29], the Dirac δ function in the singular force distribution is replaced by a regularized δ function, which leads to a smooth distribution of forces. Necessarily, this implies that the force is now no longer localized on the manifold but is sharply peaked and smooth around it. This smooth force density can now be sampled on the grid using the discretized δ function as an interpolant. Thus a representation of Eq. (22) on the grid is obtained from

$$\mathbf{F}(\mathbf{r}) = \sum_a \mathbf{f}(\mathbf{R}_a)\delta^p(\mathbf{r}-\mathbf{R}_a). \tag{23}$$

The crucial ingredient here is the kernel function δ^p, which is a representation of the Dirac δ function regularized on the grid. We have followed closely the method described by Peskin [29] where a regularized approximation to the Dirac δ function with compact support is derived:

$$\delta^p(\mathbf{r}) = \frac{1}{h^3} f\left(\frac{x}{h}\right) f\left(\frac{y}{h}\right) f\left(\frac{z}{h}\right), \tag{24}$$

where $h=\Delta x=\Delta y=\Delta z$ is the lattice spacing and $f(r)$ is given by

$$f(r) = \begin{cases} \dfrac{3-2|r|+\sqrt{1+4|r|-4r^2}}{8}, & |r| \leqslant 1, \\ \dfrac{5-2|r|-\sqrt{-7+12|r|-4r^2}}{8}, & 1 \leqslant |r| \leqslant 2, \\ 0, & |r| \geqslant 2. \end{cases} \tag{25}$$

This form is motivated by the need to preserve the fundamental properties of the Dirac δ function on the grid [29]. A simple closed form approximation to δ^p which is useful for analytical work is

$$\tilde{f}(r) = \begin{cases} \dfrac{1}{4}\left[1+\cos\left(\dfrac{\pi r}{2}\right)\right], & |r| \leqslant 2, \\ 0, & |r| > 2, \end{cases} \tag{26}$$

whose Fourier transform is given by

$$\tilde{f}(k) = \mathrm{sinc}4\pi k + \frac{1}{2}\mathrm{sinc}(4\pi k - \pi) + \frac{1}{2}\mathrm{sinc}(4\pi k + \pi). \tag{27}$$

In this work we combine Eq. (22) directly with the numerical method described in the previous section, giving a well-defined method for incorporating singular and/or off-lattice force densities into the lattice Boltzmann hydrodynamics.

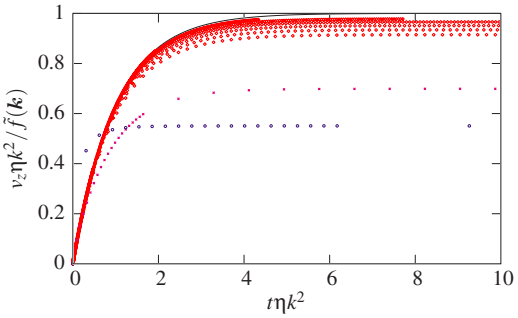

FIG. 1. (Color online) Relaxation of the solenoidal component of the velocity due to a δ function forcing. The simulations were performed on a 64^3 lattice. Shown are the first eight (upper curves), the 16th (middle curve), and the 31st (lowest curve) Fourier modes of the velocity field. The solid line is the analytical result, Eq. (29).

A. Validation

To validate the method, we compare analytical solutions of the singularly forced Navier-Stokes equation against our numerical solutions, using lattice units $\Delta x=\Delta t=1$, $\rho=1$. The most straightforward benchmark is against the initial value problem for the Stokes limit,

$$\partial_t \mathbf{v} = -\nabla p + \eta\nabla^2\mathbf{v} + \mathbf{F}(\mathbf{r}), \tag{28}$$

where the nonlinearity has been discarded, incompressibility is assumed, and $\mathbf{F}(\mathbf{r})=\mathbf{F}_0\delta(\mathbf{r}-\mathbf{R}_0)$. In an infinite system, the solution is obtained in terms of the unsteady Oseen tensor describing the diffusion of vorticity [30]. In a system with periodic boundary conditions, the Oseen solution must be replaced by the Hasimoto solution [31]. In contrast to the Oseen solution, the real-space Hasimoto solution is not available in a simple closed form but must be evaluated numerically. However, the solution in Fourier variables presents no such difficulty, and is in fact identical in both cases:

$$\mathbf{v}(\mathbf{k},t) = \frac{1-e^{-\eta k^2 t}}{\eta k^2}(\mathbb{1}-\hat{\mathbf{k}}\hat{\mathbf{k}})\cdot\mathbf{F}(\mathbf{k}). \tag{29}$$

Thus, we find it most convenient to compare Fourier modes of the velocity from the numerical solution against the solution above. In particular, this provides a neat way to evaluate the performance of the method at different length scales. In Fig. 1 we compare the numerical data (points) to the theoretical result for a regularized force monopole using the approximation to the Peskin δ function, Eq. (27) (solid line).

The results show excellent agreement with the theoretical curve for low-k modes, where we expect the momentum to behave hydrodynamically. The departure from hydrodynamic behavior increases progressively with the wave number, as expected from previous studies on the hydrodynamic behavior of the LBE [32]. However, there is a significant range of length scales over which our model reproduces hydrodynamic behavior, which is not less than the scale over which hydrodynamic behavior is obtained in the unforced LBE [33].

By combining elementary monopoles, discrete representations of higher multipoles can be generated. For example, the discrete Stokes doublet, a dipole of two point forces, can be

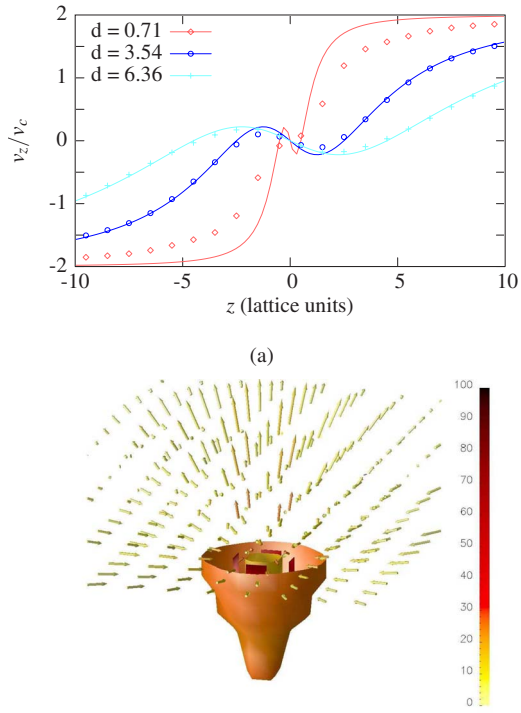

FIG. 2. (Color online) Velocity around a symmetric point-force dipole, normalized by a characteristic speed for that distance from the dipole, $v_c \equiv Fa/8\pi\eta r^2$. (a) shows velocity along lines parallel to the forces, at several separations. Points are simulation results, lines theoretical predictions with no free parameters. In (b), the upper half shows the simulated velocity field. The lower half shows isosurfaces of the magnitude of the velocity difference between simulation and theory at values of 25% and 50%. The coloring (online) depends upon the magnitude of the difference field and is shown as a percentage of v_c in the color bar. The force dipole is oriented vertically and positioned in the center of the volume.

constructed out of monopoles of magnitude F and separation a and is often used as a simplified representation of a neutrally buoyant, steadily moving self-propelled particle. In Figs. 2(a) and 2(b), we compare the velocity response of such a dipole to theoretical predictions, finding good agreement away from the immediate vicinity of the forces. In Fig. 3, we show a velocity field plot for the antisymmetric force dipole, or rotlet, which may be used as a representation of an object which rotates due to an external torque. This requires the use of four, rather than two, point forces; we arrange these in a swastikalike fashion (whose axes can be aligned in an arbitrary direction without significantly affecting the flow produced). This cancels a spurious stresslet component that arises from our regularization of the δ function for any dipole in which the forces are not collinear with the separation vector.

The above examples show that the regularized δ function provides a useful way of incorporating arbitrary distributions of singular forces into the lattice Boltzmann method, capable of dealing with internal as well as external forcing.

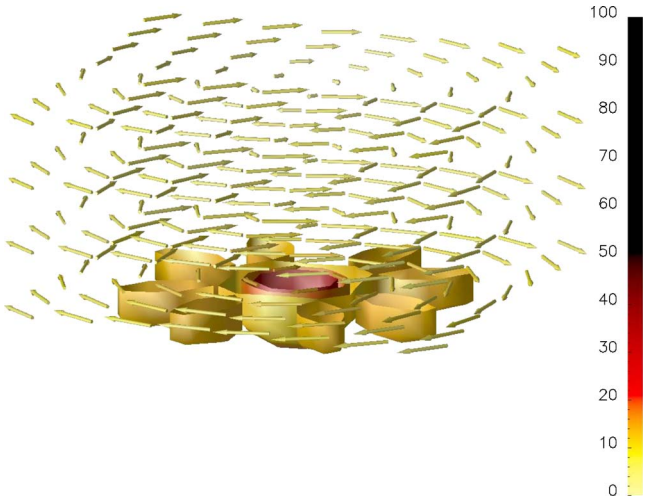

FIG. 3. (Color online) Velocity field around a regularized rotlet, normalized by v_c (see Fig. 2). Upper half: simulated velocity field. Lower half: isosurfaces of the magnitude of the velocity difference between simulation and theory. Isosurfaces are at values of 12.5%, 25%, and 37.5%. The coloring (online) depends upon the magnitude of the difference field and is shown as a percentage of v_c in the color bar. The rotlet is oriented with the forces in a horizontal plane and positioned in the center of the volume.

IV. A STOKESLET MODEL FOR DILUTE COLLOIDS

The dynamics in a dilute sedimenting suspension, despite a century of investigation, still presents open questions [20]. The problem, even for a hard-sphere suspension, is unusually difficult due to the long-ranged, many-body nature of the hydrodynamic interaction. Moreover, the flow can develop structural features at large length scales, and the role of inertia, while usually negligible at the particle scale, may be significant at those scales [34]. The Stokes approximation of globally vanishing Reynolds number cannot thus be justified *a priori* in a sedimenting suspension. The full hydrodynamic problem including inertia for both fluid and particles was first simulated by Ladd using a novel lattice Boltzmann (LB) method [35]. This method, though possibly the most competitive for fully resolved particles, remains computationally expensive. A considerable simplification of the hydrodynamics is possible if only the lowest-order multipole of the force distribution induced on the particle surface by the no-slip boundary condition is retained. This principle was exploited previously to develop representations of polymers as strings of point particles which were then coupled to an LB fluid [5,36]. A similar idea has been used [37,38] to represent resolved colloids with a mesh of point particles covering their surfaces, and in related representations of spherical and aspherical colloids via immersed boundary techniques [39–43]. However, in the current work we simplify further, treating each colloid as a single point particle (thereby sacrificing all near-field effects). The possible efficiency gains from this approach are considered in Sec. V below.

In the colloidal context, this type of model was first introduced by Saffman [11]; the finite-sized particles are replaced by a singular force monopole, the Stokeslet, located at the

nominal center of the particle. In Saffman's original model, both the fluid and the particles have no inertia. In keeping with the comments above, our model retains inertia for the fluid, while neglecting it for the particle and for hydrodynamics at the particle scale. We thus have a momentum balance equation,

$$\rho\partial_t \mathbf{v} = -\nabla p + \eta\nabla^2\mathbf{v} + \sum_s \mathbf{F}_s\delta(\mathbf{r}-\mathbf{R}_s), \tag{30}$$

where the sum includes contributions from the $s=1,\ldots,N$ particles located at $\mathbf{R}_s$ and acted upon by *external* forces $\mathbf{F}_s$. In the absence of particle inertia accelerations vanish, and the particle coordinates are updated directly using the first Faxén relation [44],

$$\dot{\mathbf{R}}_s = \mathbf{v}^\infty(\mathbf{R}_s) + \frac{\mathbf{F}_s}{6\pi\eta a}, \tag{31}$$

which relates the center of mass velocity of the particle $\dot{\mathbf{R}}_s$ to the external force on it, $\mathbf{F}_s$. The background velocity $\mathbf{v}^\infty(\mathbf{R}_s)$ is the fluid velocity at the location $\mathbf{R}_s$ *in the absence* of the sth particle. The above two equations provide a complete specification of a model of sedimenting spheres, valid in the dilute limit, for dynamics at long wavelengths.

The lattice Boltzmann implementation of this model proceeds by first replacing the Dirac δ function with the regularized δ functions to obtain a force density at the grid points $\mathbf{F}(\mathbf{r})=\Sigma_s\mathbf{F}_s\delta^p(\mathbf{r}-\mathbf{R}_s)$. Since the LBE evolves the total fluid velocity $\mathbf{v}(\mathbf{r})$ due to all particles, the background fluid velocity $\mathbf{v}^\infty$ must be obtained by a careful subtraction procedure. In the absence of fluid inertia at the particle scale this can be accomplished as follows. By definition, the fluid velocity at a node $\mathbf{v}(\mathbf{r})$ is the sum of the background velocity at the node $\mathbf{v}^\infty(\mathbf{r})$ and the velocity due to the sth Stokeslet located at $\mathbf{R}_s$, $\mathbf{v}(\mathbf{r})=\mathbf{v}^\infty(\mathbf{r})+\mathbf{v}_s(\mathbf{r},\mathbf{R}_s)$. The background velocity field at the location of the particle can be obtained using the same interpolation kernel as used for the force, $\mathbf{v}^\infty(\mathbf{R}_s)=\Sigma_\mathbf{r}\mathbf{v}^\infty(\mathbf{r})\delta^p(\mathbf{R}_s-\mathbf{r})$, and using the previous relation can be written as

$$\mathbf{v}^\infty(\mathbf{R}_s) = \mathbf{v}(\mathbf{R}_s) - \sum_\mathbf{r} \mathbf{v}_s(\mathbf{r},\mathbf{R}_s)\delta^p(\mathbf{R}_s-\mathbf{r}). \tag{32}$$

Appealing only to linearity and dimensional analysis, the sum above can be expressed as

$$\sum_\mathbf{r} \mathbf{v}_s(\mathbf{r},\mathbf{R}_s)\delta^p(\mathbf{R}_s-\mathbf{r}) \equiv \frac{\mathbf{F}_s}{6\pi\eta a_L(\mathbf{R}_s)}. \tag{33}$$

In Appendix A, we derive this result and show that the lattice parameter a_L depends only on the system size L and on the form of the regularization and interpolation kernels; it is independent of viscosity η and of the radius a. Using Eq. (33), the update equation for the Stokeslet positions can now be expressed in terms of the interpolated fluid velocity, without any reference to the background velocity,

$$\dot{\mathbf{R}}_s = \mathbf{v}(\mathbf{R}_s) + \frac{\mathbf{F}_s}{6\pi\eta}\left(\frac{1}{a} - \frac{1}{a_L(\mathbf{R}_s)}\right). \tag{34}$$

Notice that replacing the background velocity in the Faxén relation with the actual fluid velocity induces an effective backflow, leading to a renormalized hydrodynamic radius,

$$\frac{1}{a_R} = \frac{1}{a} - \frac{1}{a_L}. \tag{35}$$

The numerics thus places a constraint $a \ll a_L$ on the allowed values of the hydrodynamic radius a. This numerical constraint encodes the condition that the grid points must be in the far field of the Stokeslet, the limit in which the background velocity can be obtained from the fluid velocity by subtracting a monopole contribution. In our simulations, we operate well within this limit.

This almost completes the description of the lattice Boltzmann implementation of our Stokeslet model of sedimenting particles. The only free parameter is the hydrodynamic radius a of the particles, which decides how fast they sediment for a given force $\mathbf{F}_s$. As shown below, the lattice parameter a_L can be calculated analytically as a function of system size. We find it convenient to fit it using a procedure described in Appendix A. Finally, to address Brownian motion of our colloids, we need to use the fluctuating LBE of [28] which imparts an appropriate thermal noise spectrum to the fluid. Because of the renormalization of a, the resulting diffusivity is generally not correct unless a further noise term is added that is the counterpart of the a_L correction. The details are explained in Appendix B.

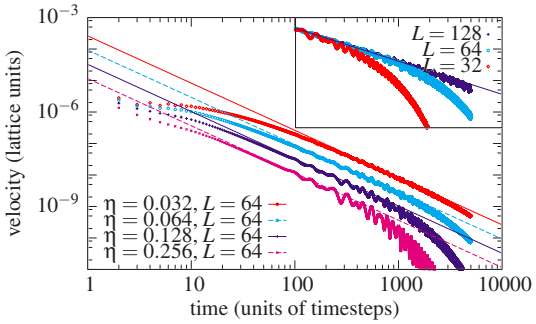

FIG. 4. (Color online) Response of a single particle to an impulsive force $\mathbf{P}$ in a periodic box. Main figure: response shown for a range of viscosities (points) compared to the theoretical prediction $\mathbf{v}=\mathbf{P}/12\rho(\pi\nu t)^{3/2}$ at long times [30]. The inset shows the effect of varying the size of the simulation box. Deviations from the prediction become significant at approximately 250, 1000, and 4000 time steps for box sizes of 32, 64, and 128, respectively. This is consistent with the expected scaling, $\tau\sim L^2/\eta$.

A. Benchmarks

Our first benchmark addresses the dynamics of a single impulsively started particle, without noise. From unsteady hydrodynamics, we know that the asymptotic decay of the particle velocity varies as $t^{-d/2}$ in d dimensions [30]. In Fig. 4 we display the decay of the particle velocity, for a single hydrodynamic radius (0.05 lattice units), but several values of the fluid viscosity. In all cases, we see the correct asymptotic behavior, until the particle begins to interact with its image, due to the periodic boundary conditions. (This interpretation is supported by the scaling of the time τ at which the deviations become significant: we find $\tau\simeq L^2/\eta$ as

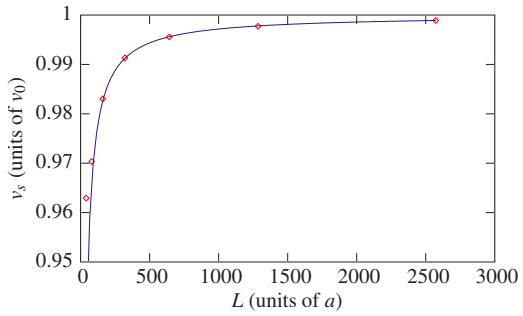

FIG. 5. (Color online) Steady sedimentation velocity of a simple cubic array of spheres, normalized by the Stokes sedimentation velocity of a single particle, v_0. The separation L is expressed in terms of the fitted particle radius a. The solid line is the theoretical result $v=v_0/(1+ka/L)$, with $k=2.84$ [31,45].

shown in the inset to Fig. 4.) In other words, our particle model correctly captures the low- and intermediate-frequency behavior of the particle mobility, but cannot capture the high-frequency behavior correctly, since that depends on the way vorticity diffuses in the immediate neighborhood of the particle, a regime that is excluded in our model.

Our next benchmark involves collective motion of a set of particles, and thus directly probes the hydrodynamic interaction between particles. In Fig. 5 the mean sedimentation velocity of a periodic array of spheres is shown, as a function of volume fraction. There is excellent agreement with the theoretical result of [45]. The model is also able to faithfully capture instabilities due to collective hydrodynamic flow. In Fig. 6 the instability of a falling two-dimensional lattice of spheres in three dimensions [46] is captured, at least qualitatively, by our model.

For most problems, all Reynolds numbers below some (situation-dependent but small) value give rise to equivalent behavior, as discussed in detail in previous work [47]. Following protocols discussed there, we have compared the normalized velocity field $\mathbf{u}=\mathbf{v}/v_0$ (with v_0 the sedimentation velocity of an isolated colloid) for a number of simulations of a single sedimenting sphere with periodic boundary conditions (see Fig. 7) in order to explore the range of Reynolds number at which our algorithm gives acceptably accurate results. Our "reference" simulation has a very small Re $=10^{-6}$ such that we can be confident it is in the Stokesian limit [47]. This is shown in Fig. 7(a). Figures 7(b) and 7(c) show the normalized velocity difference fields between the reference case and simulations with Re$=10^{-4}$ and 10^{-2}, respectively. In the simulation with Re$=10^{-4}$, the magnitude of the difference is everywhere less than 2×10^{-5}, a negligibly small error. In the simulation with Re$=10^{-2}$, we find $|\Delta\mathbf{u}|$ $\leqslant 0.01$ throughout the bulk of the domain; only in the immediate vicinity of the particle does it become larger. This suggests that this Reynolds number is sufficiently low to give "realistic," although not "fully realistic," behavior [47]. Since reaching very low Reynolds number requires paying a larger cost in computational time, and there are other sources of percent-level error in the code, Re$=10^{-2}$ is probably a reasonable compromise between accuracy and run time, for studies in the low-Reynolds-number limit.

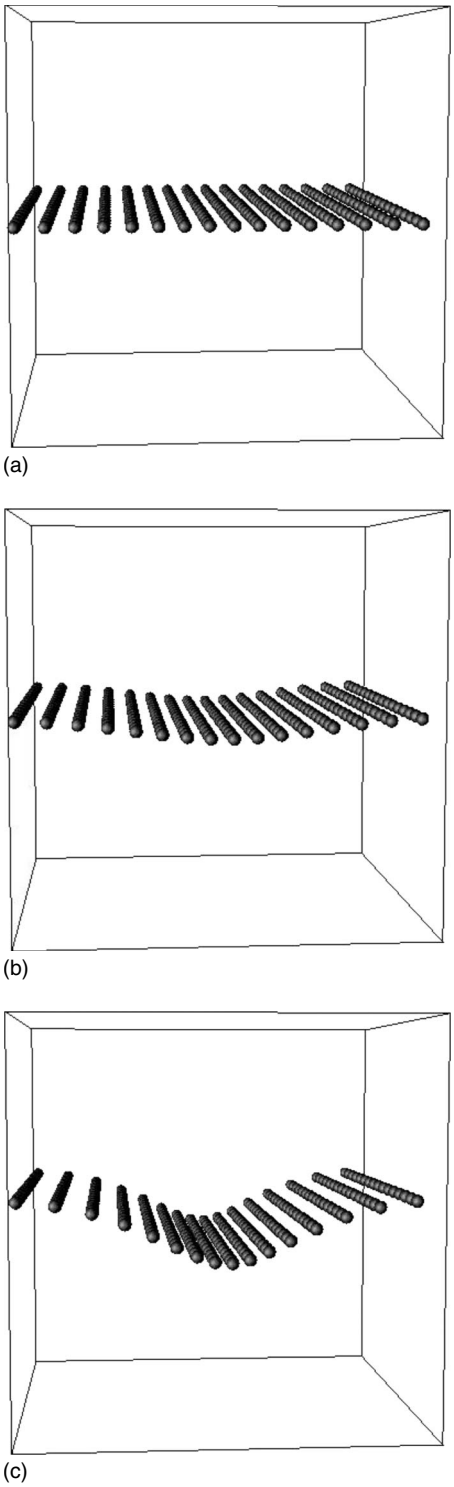

FIG. 6. Crowley instability of a two-dimensional lattice of sedimenting particles. Images are generated in the comoving frame and particle size has been exaggerated for illustrative purposes. Images taken at times of $t=$ (a) $0t_{\mathrm{St}}$, (b) $1650t_{\mathrm{St}}$, and (c) $3300t_{\mathrm{St}}$.

B. Comparison to a fully resolved LB algorithm

As a final benchmark, we have compared the behavior of our sedimenting particle model with a fully resolved colloid simulation code using the algorithm of Nguyen and Ladd

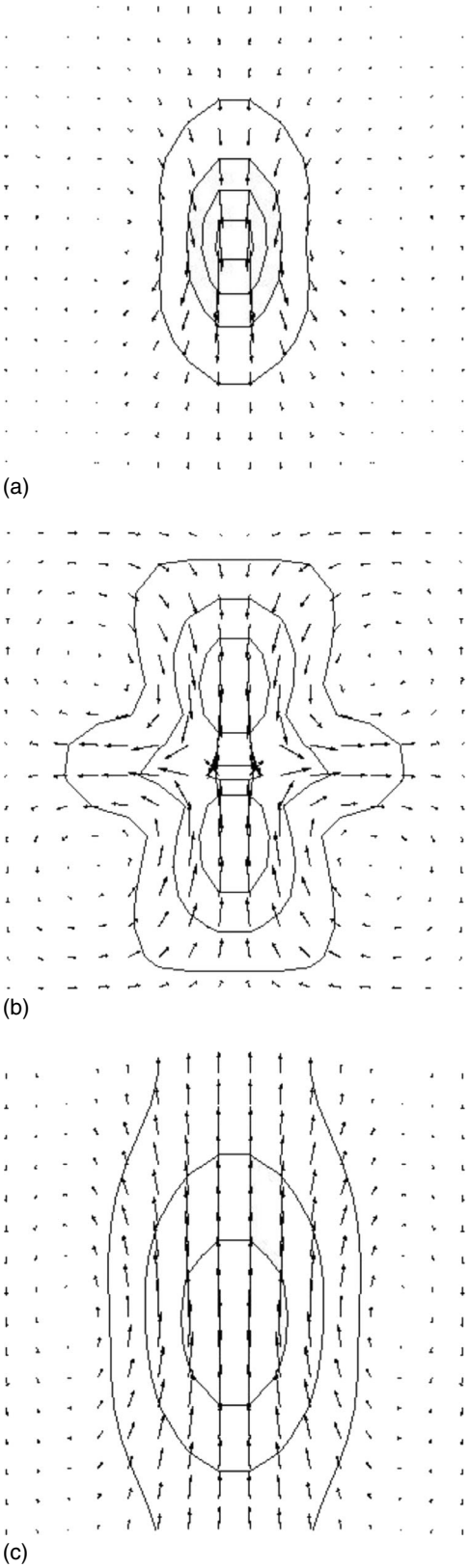

FIG. 7. Contour plots of (a) the normalized velocity field **u** for a reference simulation at very low $\mathrm{Re}=10^{-6}$; and velocity difference fields for $\mathrm{Re}=$(b)10^{-4} and (c) 10^{-2}. These are for a pointlike colloid sedimenting in a 32^3 box with periodic boundary conditions. Reference case: contour interval $0.02v_0$. $\mathrm{Re}=10^{-4}$ case: contour interval 5×10^{-6}. $\mathrm{Re}=10^{-2}$ case: contour interval 5×10^{-3}.

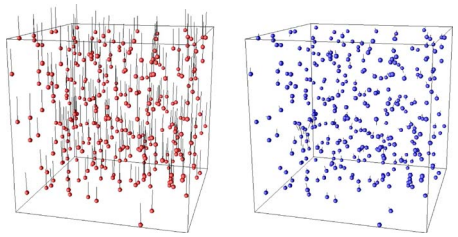

FIG. 8. (Color online) Both visualizations show the particles at their position in the point-particle simulation after ten Stokes times. Left: lines show the trajectories from the starting configuration. Right: lines show the difference between fully resolved and pointlike algorithms. Parameters for the two systems are shown in Table I. See also Movie 1 [50].

[48]. (For full implementation details, see [49].) At dilute concentrations, the paths of the particles are almost indistinguishable between the two simulations when plotted graphically. This is shown in Fig. 8 for volume fraction $\phi=3.0\times10^{-3}$; note that the largest differences occur when the density of particles is large locally, when the implicit assumption of our model that the particles are always at separations large compared to their radius is no longer valid. We cannot expect both simulations to give the same trajectories for long times, since the small differences between algorithms will cause exponential separation of trajectories owing to the positive Lyapunov exponent of the system. However, from a plot of the mean difference in position between the two simulations against time, we can see excellent agreement for several Stokes times, and until at least ten Stokes times for sufficiently dilute systems (Fig. 9).

V. DISCUSSION

The focus of this work has been to derive and validate a general method for addressing singular forcing in the LBE, with specific application to the simulation of pointlike particles. We have shown the method to agree well with analytic results, where available, and with fully resolved particle algorithms at low concentrations and Reynolds number (Secs. III A, IV A, and IV B).

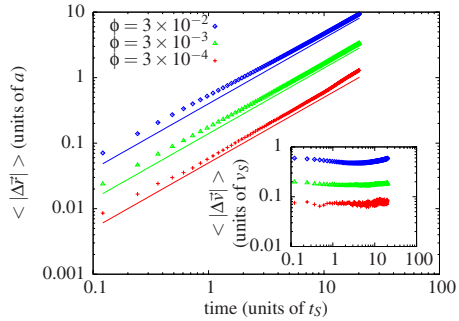

FIG. 9. (Color online) Main figure: mean absolute difference in position between fully resolved and pointlike sedimenting particles. Inset: mean absolute difference in velocity between the two simulations. Parameters for the two systems are shown in Table I.

TABLE I. Parameters for simulations used to compare fully resolved and pointlike algorithms; see text and Figs. 8 and 9.

Parameter	Fully resolved	Point particle
Lattice size L	96	9
Particle radius a	1.25	0.117
Viscosity η	1/6	1/6
Density ρ	1.0	1.0
Reynolds number Re	0.01	0.01
Stokes time τ_S	937	8
Number of particles	321	321
Volume fraction ϕ	3.0×10^{-3}	3.0×10^{-3}

Additionally, due to its careful construction, the regularized δ function provides a good interpolation scheme, minimizing velocity fluctuations as the particle moves relative to the computational grid. Indeed, we find that for sedimenting colloids, the trajectories are much smoother in our Stokeslet algorithm than for the fully resolved simulation. In the latter, the discretization renders particles hydrodynamically aspherical with shapes that vary as they move across the lattice [49].

Other approaches to adding particles can also reduce the errors due to shape changes as the particles move, for example the immersed-boundary–lattice-Boltzmann method [39–43], LBM for immiscible liquids [51], or finite-difference methods coupled to Stokes equation solutions near the particle [52]. These methods can also deal with aspherical and/or deformable colloidal particles. However, they all involve fully resolving the particle boundaries and thus require particle radii at least as big as in Ladd's algorithm: for a given number and concentration of particles, they should therefore require comparable computational effort (which is dominated in practice by the LBE sector for the bulk fluid). In contrast, with our point-particle algorithm, as shown in Table I, similar particle numbers and volume fractions can be simulated with a LB lattice that is smaller in linear dimension by a factor $\lambda\approx10$. (This is the ratio of the particle radii in the two simulations.) The computational time to update the particle positions is essentially negligible, so that the CPU time needed to perform one LB time step is decreased by a factor of λ^3; moreover, the Stokes time $\tau_S=\rho a^2/\eta\mathrm{Re}$ scales as λ^2. The latter sets the time basic time scale for evolution of sedimentation trajectories, so that for this problem we expect a speedup of $O(\lambda^5)\approx10^5$. This should allow us to study the sedimentation behavior of dilute systems with tens of millions of particles. This scaling to very large systems should allow us to accurately determine the long-wavelength particle structure factor, which is a quantity of great theoretical interest [12]. This structure factor determines the ultimate character of the sedimentation dynamics, which depends on how particles become correlated over length scales large compared to their mean separation. Even the largest fully resolved LB simulations [53] currently have difficulty addressing this regime, which we hope to address in future work using our method.

Generalizations of our algorithm to more complicated, but still pointlike, objects should prove relatively straightforward. By calculating the coefficients of higher-order multipoles, the force distribution for objects such as nonspherical or self-propelled particles (e.g., motile bacteria) might be included within the framework of pointlike objects. To simulate polymeric structures, one might make the driving force on each particle the sum of bonding interactions between it and its neighbors. Further, the accuracy of our Stokeslet model can be increased by including higher-order terms of the surface force distribution. In particular, a second-order (Rotne-Prager) term could improve accuracy for colloids, and with some geometries and/or boundary conditions might prove important, even in the dilute limit [54,55]. However, our comparisons with the resolved particle simulations suggest that this term is not crucial under the conditions we have studied.

Although the aforementioned methods [6,39–43,51,52] have a larger domain of applicability than our code, particularly for situations with high volume fractions and finite particle Reynolds number, in the limit of dilute suspensions when only low-order multipoles are significant, our approach might prove preferable, even for aspherical particles, due to its much greater computational efficiency. We note that spectral methods offer another approach to include point forces in fluid simulations [55]; however, they require a different Green's function for each different boundary condition and are restricted to relatively simple geometries. As with all LBE-based codes, the absence of such restrictions is an attractive feature of our approach.

ACKNOWLEDGMENTS

We thank Kevin Stratford and Tony Ladd for useful discussions, and K. Vijay Kumar for communications on the Crowley instability. The work was funded in part by EPSRC Grant No. GR/S10377.

APPENDIX A: SUBTRACTION PROCEDURE

We derive here the correction factor that arises from replacing the background velocity with the fluid velocity in the Faxén relation. The velocity at a node due to a regularized Stokeslet located at $\mathbf{R}_s$ is

$$\mathbf{v}_s(\mathbf{r},\mathbf{R}_s)=\frac{1}{L^3}\sum_{\mathbf{k}\neq\mathbf{0}}\frac{e^{i\mathbf{k}\cdot\mathbf{r}}}{\eta k^2}\delta^p(\mathbf{k};\mathbf{R}_s)(\mathbb{1}-\hat{\mathbf{k}}\hat{\mathbf{k}})\cdot\mathbf{F}_s. \quad \text{(A1)}$$

This velocity interpolated from the neighboring nodes to the location of the particle is

$$\sum_{\mathbf{r}}\mathbf{v}^s(\mathbf{r},\mathbf{R}_s)\delta^p(\mathbf{r}-\mathbf{R}_s)=\mathbf{F}_s\cdot\sum_{\mathbf{r},\mathbf{k}\neq\mathbf{0}}\frac{e^{i\mathbf{k}\cdot\mathbf{r}}}{\eta k^2}\frac{\delta^p(\mathbf{k};\mathbf{R}_s)}{L^3}\times(\mathbb{1}-\hat{\mathbf{k}}\hat{\mathbf{k}})\delta^p(\mathbf{r}-\mathbf{R}_s). \quad \text{(A2)}$$

Completing the spatial sum, we get for the interpolated Stokeslet velocity

$$\sum_{\mathbf{r}} \mathbf{v}_s(\mathbf{r},\mathbf{R}_s)\,\delta^P(\mathbf{r}-\mathbf{R}_s) = \mathbf{F}_s \cdot \sum_{\mathbf{k}\neq\mathbf{0}} \frac{|\delta^P(\mathbf{k};\mathbf{R}_s)|^2}{\eta k^2}(\mathbb{1}-\hat{\mathbf{k}}\hat{\mathbf{k}}) \equiv \frac{\mathbf{F}_s}{6\pi\eta a_L(\mathbf{R}_s)}, \tag{A3}$$

which shows that the offset parameter a_L obeys

$$\frac{1}{a_L(\mathbf{R}_s)} = \frac{6\pi}{L^3}\sum_{\mathbf{k}\neq\mathbf{0}} \frac{|\delta^P(\mathbf{k};\mathbf{R}_s)|^2}{k^2}(\mathbb{1}-\hat{\mathbf{k}}\hat{\mathbf{k}}); \tag{A4}$$

it is indeed independent of viscosity and particle radius a, but depends on the lattice size L and the numerical implementation of the regularization and interpolation.

APPENDIX B: NOISE

Considering a spherical sedimenting particle in the Langevin picture, we can write

$$m\ddot{\mathbf{R}} = -6\pi\eta a(\dot{\mathbf{R}}-\mathbf{v}^\infty) + \mathbf{F} + \zeta(t), \tag{B1}$$

and taking the inertialess limit gives

$$\dot{\mathbf{R}} = \mathbf{v}^\infty(\mathbf{R}) + \frac{\mathbf{F}}{6\pi\eta a} + \zeta(t). \tag{B2}$$

We note that, in this equation, noise comes in only through the Gaussian random variable ζ and that in particular the fluid velocity $\mathbf{v}^\infty$ is completely deterministic.

The update rule for our model particle is

$$\dot{\mathbf{R}} = \mathbf{v}(\mathbf{R}) - \frac{\mathbf{F}}{6\pi\eta a_L} + \frac{\mathbf{F}}{6\pi\eta a}, \tag{B3}$$

which is sufficient for the infinite-Péclet-number regime. If one uses a fluctuating LB method, then the interpolated velocity $\mathbf{v}(\mathbf{R})$ contains a noise component. However, we do not expect the magnitude of the noise to be appropriate for a particle of the desired radius a, since the random component of the velocity has no dependence on the radius of the particle. In fact, the variance of this noise is that expected for a Brownian particle with the same radius as the offset parameter a_L ($>a$), and we use this fact to determine its value from a diffusion "experiment" on an unforced particle, as explained below.

Knowing that the particle will otherwise diffuse as one with a much larger radius, we add a white noise term to the update rule for the model,

$$\dot{\mathbf{R}} = \mathbf{v}(\mathbf{R}) - \frac{\mathbf{F}}{6\pi\eta a_L} + \frac{\mathbf{F}}{6\pi\eta a} + \zeta'(t). \tag{B4}$$

The variance of the extra noise is determined by the requirement of satisfying the fluctuation-dissipation theorem to be

$$\langle \zeta_i'(t)\zeta_j'(t')\rangle = \frac{kT}{3\pi\eta}\left(\frac{1}{a}-\frac{1}{a_L}\right)\delta_{ij}\delta(t-t'). \tag{B5}$$

To determine the value of the offset parameter a_L, we set up a simulation of a single unforced particle in periodic boundary conditions at finite temperature and disable the extra noise term discussed above, giving

$$\dot{\mathbf{R}} = \mathbf{v}(\mathbf{R}) \tag{B6}$$

as the equation of motion of the particle.

We let the simulation equilibrate for the characteristic time for momentum to diffuse across the box size, TL^2/η, before recording the displacement as a function of time. This is repeated for a number of different starting positions relative to the LB grid, and a plot of $\langle \mathbf{r}^2\rangle$ vs t is used to estimate the diffusivity. We then use the Stokes-Einstein relation to derive a radius and use this as the offset parameter. We then test to ensure that this gives the correct sedimentation behavior of a particle.

[1] S. Succi, *The Lattice Boltzmann Equation, For Fluid Dynamics and Beyond* (Oxford University Press, Oxford, 2001).
[2] X. Shan and H. Chen, Phys. Rev. E **47**, 1815 (1993).
[3] X. Shan and H. Chen, Phys. Rev. E **49**, 2941 (1994).
[4] M. R. Swift, E. Orlandini, W. R. Osborn, and J. M. Yeomans, Phys. Rev. E **54**, 5041 (1996).
[5] P. Ahlrichs and B. Dunweg, Int. J. Mod. Phys. C **9**, 1429 (1998).
[6] A. J. C. Ladd, J. Fluid Mech. **271**, 285 (1994).
[7] A. J. C. Ladd, J. Fluid Mech. **271**, 311 (1994).
[8] J. M. Buick and C. A. Greated, Phys. Rev. E **61**, 5307 (2000).
[9] P. Résibois and M. Leener, *Classical Kinetic Theory of Fluids* (John Wiley, New York, 1977).
[10] M. Doi and S. F. Edwards, *The Theory of Polymer Dynamics* (Clarendon Press, Oxford, 1986).
[11] P. G. Saffman, Stud. Appl. Math. **52**, 115 (1973).
[12] S. Ramaswamy, Adv. Phys. **50**, 297 (2001).
[13] X. He and L.-S. Luo, Phys. Rev. E **55**, R6333 (1997).
[14] X. Shan and X. He, Phys. Rev. Lett. **80**, 65 (1998).
[15] X. Shan, X.-F. Yuan, and H. Chen, J. Fluid Mech. **550**, 413 (2006).
[16] T. Lee and C.-L. Lin, J. Comput. Phys. **171**, 336 (2001).
[17] T. Lee and C.-L. Lin, J. Comput. Phys. **185**, 445 (2003).
[18] S. Chen and G. D. Doolen, Annu. Rev. Fluid Mech. **30**, 329 (1998).
[19] N. Cao, S. Chen, S. Jin, and D. Martínez, Phys. Rev. E **55**, R21 (1997).
[20] A. J. C. Ladd and R. Verberg, J. Stat. Phys. **104**, 1191 (2001).
[21] X. Y. He and L. S. Luo, Phys. Rev. E **56**, 6811 (1997).
[22] Y. Qian, D. d'Humieres, and P. Lallemand, Europhys. Lett. **17**, 479 (1992).
[23] N. S. Martys, X. Shan, and H. Chen, Phys. Rev. E **58**, 6855 (1998).
[24] X. He, X. Shan, and G. Doolen, Phys. Rev. E **57**, R13 (1998).
[25] D. Zwillinger, *Handbook of Differential Equations*, 3rd ed. (Academic Press, London, 1998).
[26] P. J. Dellar, Phys. Rev. E **64**, 031203 (2001).
[27] Z. L. Guo, C. Zheng, and B. C. Shi, Phys. Rev. E **65**, 046308

(2002).
[28] R. Adhikari, K. Stratford, A. J. Wagner, and M. E. Cates, Europhys. Lett. **71**, 473 (2005).
[29] C. S. Peskin, Acta Numerica **11**, 479 (2002).
[30] L. D. Landau and E. M. Lifshitz, *Fluid Mechanics* (Pergamon, Moscow, 1971).
[31] H. Hasimoto, J. Fluid Mech. **5**, 317 (1959).
[32] P. Lallemand and L. S. Luo, Phys. Rev. E **61**, 6546 (2000).
[33] O. Behrend, R. Harris, and P. B. Warren, Phys. Rev. E **50**, 4586 (1994).
[34] P. N. Segre, E. Herbolzheimer, and P. M. Chaikin, Phys. Rev. Lett. **79**, 2574 (1997).
[35] A. J. C. Ladd, Phys. Rev. Lett. **70**, 1339 (1993).
[36] O. B. Usta, A. J. C. Ladd, and J. Butler, J. Chem. Phys. **122**, 094902 (2005).
[37] V. Lobaskin and B. Dünweg, New J. Phys. **6**, 54 (2004).
[38] V. Lobaskin, B. Dünweg, and C. Holm, J. Phys.: Condens. Matter **16**, S4063 (2004).
[39] Z.-G. Feng and E. Michaelides, J. Comput. Phys. **195**, 602 (2004).
[40] Z.-G. Feng and E. Michaelides, J. Comput. Phys. **202**, 20 (2005).
[41] Y. Peng, C. Shu, Y. Chew, X. Niu, and X. Lu, J. Comput. Phys. **218**, 460 (2006).
[42] M. Uhlmann, J. Comput. Phys. **209**, 448 (2005).
[43] X. Shi and N. Phan-Thien, J. Comput. Phys. **206**, 81 (2005).
[44] C. Pozrikidis, *Boundary Integral and Singularity Methods for Linearized Viscous Flow* (Cambridge University Press, Cambridge, U.K., 1992).
[45] J. Happel and H. Brenner, *Low Reynolds Number Hydrodynamics* (Prentice-Hall, London, 1965).
[46] J. M. Crowley, Phys. Fluids **19**, 1296 (1976).
[47] M. E. Cates, K. Stratford, R. Adhikari, P. Stansell, J. C. Desplat, and I. Pagonabarraga, J. Phys.: Condens. Matter **16**, S3903 (2004).
[48] N.-Q. Nguyen and A. J. C. Ladd, Phys. Rev. E **66**, 046708 (2002).
[49] K. Stratford, R. Adhikari, I. Pagonabarraga, and J. C. Desplat, J. Stat. Phys. **121**, 163 (2005).
[50] See EPAPS Document No. E-PLEEE8-77-057802 for an animated movie of Fig. 8. For more information on EPAPS, see http://www.aip.org/pubservs/epaps.html.
[51] T. Inamuro and T. Ii, Math. Comput. Simul. **72**, 141 (2006).
[52] Z. Zhang and A. Prosperetti, J. Comput. Phys. **210**, 292 (2005).
[53] N.-Q. Nguyen and A. Ladd, J. Fluid Mech. **525**, 73 (2005).
[54] A. J. C. Ladd (private communication).
[55] P. Mucha, D. Weitz, B. Shraiman, and M. Brenner, J. Fluid Mech. **501**, 71 (2004).